Nodal loop and nodal surface states in the Ti_3Al family of materials

Xiaoming Zhang,[1,2,*] Zhi-Ming Yu,[2] Ziming Zhu,[2] Weikang Wu,[2] Shan-Shan Wang,[2]
Xian-Lei Sheng,[3] and Shengyuan A. Yang[2,†]

[1]*School of Materials Science and Engineering, Hebei University of Technology, Tianjin 300130, China*
[2]*Research Laboratory for Quantum Materials, Singapore University of Technology and Design, Singapore 487372, Singapore*
[3]*Department of Applied Physics, Key Laboratory of Micro-nano Measurement-Manipulation and Physics (Ministry of Education), Beihang University, Beijing 100191, China*

(Received 6 May 2018; revised manuscript received 19 June 2018; published 28 June 2018)

Topological metals and semimetals are new states of matter which are attracting great interest in current research. Here, based on first-principles calculations and symmetry analysis, we propose that the family of titanium-based compounds Ti_3X (X=Al, Ga, Sn, Pb) are unexplored topological metals. These materials feature the coexistence of a nodal loop and a nodal surface in their low-energy band structures. Taking Ti_3Al as an example, we show that the material has an almost ideal nodal loop in the sense that the loop is close to the Fermi level and it is nearly flat in energy with energy variation < 0.25 meV. The loop is protected by one of the two independent symmetries: the combined space-time-inversion symmetry and the mirror-reflection symmetry. The nodal surface at the $k_z = \pi$ plane is guaranteed by the nonsymmorphic screw rotational symmetry and the time-reversal symmetry. We discuss the effect of spin-orbit coupling and construct an effective model for describing the nodal loop. Our findings indicate that the Ti_3Al family of compounds can serve as an excellent material platform for studying new topological phases and, particularly, the interplay between nodal loop and nodal surface fermions.

DOI: 10.1103/PhysRevB.97.235150

I. INTRODUCTION

Crystalline solids may have nontrivial topology encoded in their electronic band structure. The exploration of this notion gives rise to the fascinating field of topological materials that has attracted tremendous interest from physics, chemistry, and materials science. Initially studied in the context of insulating states [1,2], now the concept of band topology has been extended to metal and semimetal states [3–5]. In these topological metals, topology is associated with the nontrivial band crossings at low energy. For example, in a Weyl semimetal [6,7], the conduction and valence bands cross at isolated nodal points, around which the band dispersion is linear in all directions and the low-energy electrons behave like Weyl fermions [8], making it possible to simulate fascinating phenomena in high-energy physics and general relativity, such as chiral anomalies [8,9], artificial black/white holes, gravitational lenses [10], and Hawking radiation [10,11]. The Weyl nodal point, acting like monopoles in the k space, is topologically robust against weak perturbation. With proper crystalline symmetry, superposing two Weyl points can make a stable Dirac nodal point, leading to a Dirac semimetal state [12–15].

For a three-dimensional system, according to the dimensionality of the band crossing, in addition to the various zero-dimensional nodal points, we can, in principle, also have one-dimensional (1D) nodal lines and two-dimensional nodal surfaces. There have been several nodal line materials proposed so far [16–33], showing rich properties. Depending on the shape, the lines may take various forms, including a single ring, multiple-crossing rings [16,34], loops traversing the Brillouin zone (BZ) [19,35], extended chains [36,37], Hopf links [38–42], nodal boxes [43], etc. The lines can also be classified based on the type of band dispersion around the crossing, which leads to the type-I, type-II, and hybrid nodal lines [35,44]. Meanwhile, the possibility of nodal surface semimetals was just noticed recently, initially by Zhong *et al.* [45] in a family of carbon network materials and by Liang *et al.* [46] in the $BaVS_3$ family of materials. Wu *et al.* [47] have proposed two classes of nodal surfaces and further provided sufficient conditions and examples for robust nodal surfaces in the presence of spin-orbit coupling (SOC) and in magnetic materials. Compared with nodal point and nodal line materials, the proposed nodal surface materials are far fewer, and there is no experimental verification of a nodal surface semimetal yet.

These topological states are expected to exhibit interesting features in their electronic, transport, optic, and magnetic properties. To study these properties, from a materials point of view, an important condition is that the nontrivial band crossing must be close to the Fermi level because most electronic properties are determined by the low-energy electrons around the Fermi level. In addition, for experimental studies as well as applications, the material should be stable and easy to synthesize. These conditions limit the suitable candidate materials, and currently, there is urgent need to search for realistic material systems for the realization of the nodal line and nodal surface topological semimetal states.

In this work, by using first-principles calculations and symmetry analysis, we show that the Ti_3Al family of compounds exhibits novel topological band structures with the coexistence of a nodal loop and a nodal surface in the low-energy

*zhangxiaoming87@hebut.edu.cn
†shengyuan_yang@sutd.edu.sg

band structures. Taking Ti_3Al as a concrete example, we show that the material has an almost ideal nodal loop in that (i) the loop is close to the Fermi level and (ii) it is almost flat in energy, with an energy variation less than 0.25 meV. Such flatness has not been seen in other proposed materials. Besides the nodal loop, Ti_3Al also hosts a nodal surface in the $k_z = \pi$ plane near the Fermi level, dictated by the nonsymmorphic screw-rotational symmetry and the time-reversal symmetry. The effect of SOC is discussed, and an effective model is constructed to describe the nodal loop. In addition, high-quality Ti_3Al has been synthesized, and the compound is known to possess other outstanding material properties, such as low density, high specific Young's modulus, high strength, and excellent corrosion, oxidation, and burn resistances [48]. Thus, our result reveals a realistic material platform for the exploration of novel properties of nodal loop and nodal surface topological states.

II. METHODS AND CRYSTAL STRUCTURE

To study the electronic properties, we carry out the first-principles calculations based on the density functional theory (DFT), using the Vienna Ab initio Simulation Package (VASP) [49,50]. The generalized gradient approximation (GGA) with the Perdew-Burke-Ernzerhof realization is used for the exchange-correlation potential [51]. The projector augmented-wave (PAW) method is used to treat the ionic potentials [52]. A plane-wave basis set with a kinetic energy cutoff of 500 eV is employed. Here, $11 \times 11 \times 11$ and $15 \times 15 \times 15$ Γ-centered k meshes are adopted for the structural optimization and the self-consistent calculations, respectively. The structures are fully relaxed until the residual forces are less than 0.001 eV/Å, and the energy convergence criterion is set to be 10^{-7} eV. To investigate the surface spectrum, we construct the maximally localized Wannier functions [53–55] and make use of the WANNIERTOOLS package [56].

Experimentally, high-quality Ti_3Al bulk crystals and nanoparticles have been synthesized by various methods [57–59]. The Ti_3Al compound naturally crystallizes in the hexagonal DO_{19} structure [57–61], with space group *P63/mmc* (No. 194). As shown in Figs. 1(a) and 1(b), in the unit cell of Ti_3Al, the bonding between Ti and Al atoms forms two chains of tetrahedrons with a $c/2$ relative shift along the z direction (c axis). The two Al atoms are at the *2c* Wyckoff sites (1/3, 2/3, 1/4) and the six Ti atoms are at the *6h* Wyckoff sites (u, $1-u$, 1/4). The optimized lattice parameters are $a = b = 5.756$ Å, $c = 4.652$ Å;, and $u = 0.8311$, which agree well with the experimental values ($a = b = 5.764$ Å, $c = 4.664$ Å, and $u = 0.8333$) [62]. The optimized lattice structure is used in the band structure calculations.

Before proceeding, we note that the crystal has the following important symmetries: inversion $\mathcal{P}$, mirror reflection $\mathcal{M}_z$, and twofold screw rotation $\mathcal{S}_{2z} : (x, y, z) \to (-x, -y, z + 1/2)$. Here, $\mathcal{S}_{2z}$ is a nonsymmorphic symmetry, which involves fractional lattice translations. In addition, no magnetic ordering is observed for the material [63], so the time-reversal symmetry $\mathcal{T}$ is also preserved.

III. ELECTRONIC STRUCTURE

The electronic band structure and the projected density of states (PDOS) for Ti_3Al are plotted in Fig. 2. Here, SOC is neglected since its strength is very small (because only light elements are involved), and its effect will be discussed later. The result in Fig. 2 shows a semimetal feature with a suppressed density of states (DOS) at the Fermi level. In addition, there is no spin polarization found in the calculation. These results are consistent with the experimental observations [63]. From the PDOS plot, we find that the states near the Fermi level are mainly contributed by the d orbitals of the Ti atoms. Notably, there exist several band crossings in the low-energy band structure near the Fermi level. First, there are two linear band-crossing points near the Γ point, which are labeled P_1 and P_2 in Fig. 2. Second, two bands cross linearly at the A point along Γ-A, and they become degenerate along the paths A-L-H-A. In the following, we shall analyze these two groups of band crossings one by one.

A. Nodal loop

Let's first consider the two linear band-crossing points P_1 and P_2. Figure 3(a) shows the enlarged band structure around the two points. One observes that the crossings are associated with the inverted band ordering (between the two crossing bands) around the Γ point. By analyzing the orbital components of the states, we find that one band mainly has d_{z^2} orbital character, whereas the other band has d_{xz} and d_{yz} orbital character. Due to the presence of both $\mathcal{P}$ and $\mathcal{T}$ symmetries,

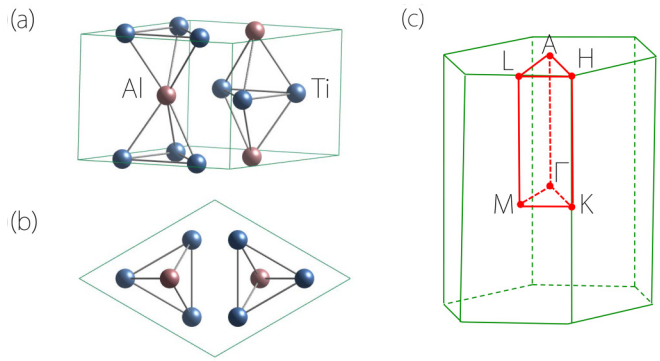

FIG. 1. Crystal structure of Ti_3Al in the (a) side view and (b) top view. (c) Brillouin zone with the considered high-symmetry points.

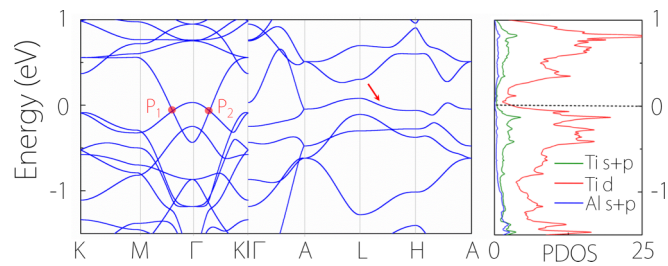

FIG. 2. Electronic band structure and the projected density of states (PDOS) for Ti_3Al. The spin-orbit coupling is neglected. The two band-crossing points labeled P_1 and P_2 are two points on a nodal loop centered around Γ. The arrow indicates the nodal surface in the $k_z = \pi$ plane.

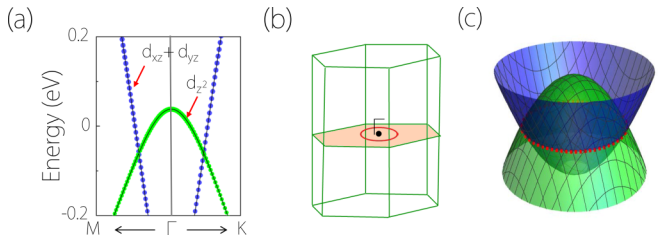

FIG. 3. (a) Orbital-projected band structure of Ti_3Al for paths near the Γ point. (b) Schematic illustration of the nodal loop in the Brillouin zone. (c) Dispersion of the bands in the $k_z = 0$ plane around Γ, showing the nodal loop.

such crossing points cannot be isolated [16]. We perform a scan of the band structure around the two points and find that the two points, in fact, sit on a nodal loop in the $k_z = 0$ plane centered at the Γ point [see Fig. 3(b)]. In Fig. 3(c), we plot the band dispersion in the $k_z = 0$ plane around Γ, and we clearly observe the nodal loop formed by the linear crossing between the two bands. This nodal loop is at an energy of about −67 meV, quite close to the Fermi level. Since it is slightly below the Fermi level, it can be readily detected in the angle-resolved photoemission spectroscopy measurement.

There is generally finite-energy variation along a nodal line (unless there is a special symmetry constraint like that for nodal loops in the superconducting excitation spectrum [17]). In the proposed nodal line materials, such variation is typically large, on the order of hundreds of meV. A salient feature of the nodal loop in Ti_3Al is that the loop is quite flat in energy. In Figs. 4(a)–4(c), we examine the energy variation for points on the loop. The result shows that the variation is less than 0.25 meV. (The numerical accuracy of our DFT calculation reaches 10^{-4} meV per unit cell. We have checked that the convergence of the band energy with respect to the number of k points and cutoff energy is better than 1×10^{-2} meV.) In comparison, the loop energy

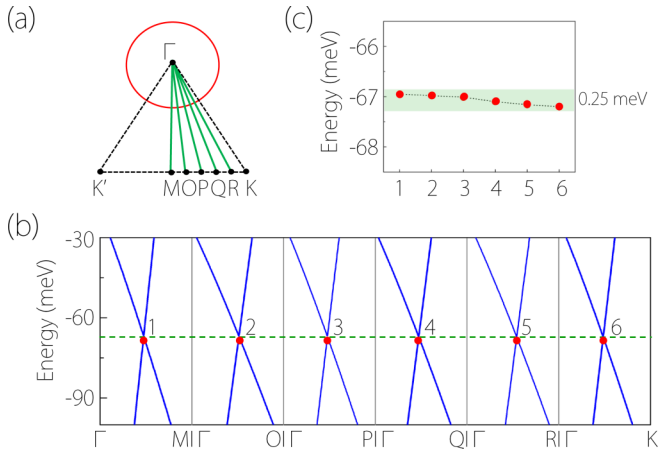

FIG. 4. (a) Schematic showing the paths taken in the $k_z = 0$ plane. The red circle denotes the nodal loop. The points O, P, Q, and R are equally spaced between M and K. (b) Band dispersions along the paths as indicated in (a). The green horizontal line serving as a guide to the eye is positioned at −65 meV. (c) Energy variation for the crossing points as shown in (b). The variation range is less than 0.25 meV.

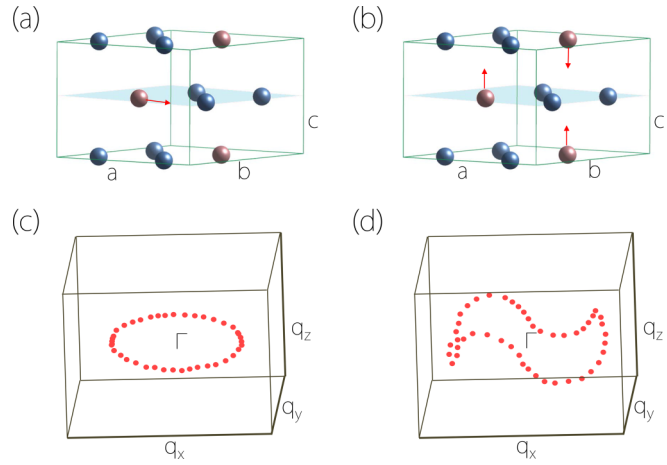

FIG. 5. (a) Breaking the inversion symmetry by shifting one of the Al atoms in the unit cell along the a axis. Note that the mirror symmetry $\mathcal{M}_z$ is preserved. (b) Breaking the mirror symmetry $\mathcal{M}_z$ by shifting the two Al atoms along the c axis in opposite directions. In this case, the inversion symmetry is preserved. (c) and (d) The schematic illustrations of the nodal loop in (a) and (b), respectively.

variation is >200 meV for Cu_3PdN [20,21], >300 meV for TiB_2 [32], and >800 meV for the elemental Be crystal [28]. Thus, the nodal loop in Ti_3Al can be regarded as exceedingly flat in energy.

As we have mentioned, nodal loops can be classified based on the dispersion type for the points on the loop. A type-I loop is formed by the crossing between an electronlike band and a holelike band; a type-II loop is formed by the crossing between two electronlike or two holelike bands [35], and a hybrid loop typically occurs when one of the crossing bands is saddlelike [44]. Here, from Figs. 3(c) and 4, we easily see that the nodal loop in Ti_3Al is type I.

The nodal loop here is robust due to the protection by two independent symmetries in the absence of SOC. The first is the combined $\mathcal{PT}$ symmetry, which requires that the Berry phase along any close path in the system must be quantized in units of π. We have numerically verified that for a path encircling the nodal loop, the Berry phase is nontrivial ($\pm\pi$ with the sign depending on the direction of the path); hence, the loop cannot be gapped out by weak perturbations that preserve the symmetry. The second protection comes from the $\mathcal{M}_z$ symmetry. The two crossing bands have opposite $\mathcal{M}_z$ eigenvalues in the mirror-invariant plane $k_z = 0$ [which can also be easily seen from their orbital characters in Fig. 3(a)]; hence, the two bands must cross without hybridization. The $\mathcal{M}_z$ symmetry also confines the loop within the $k_z = 0$ plane.

It should be noted that the two protections are independent, which means that the loop is robust as long as one of them is preserved. To explicitly demonstrate this point, we consider the following perturbations to the lattice structure. In the first case, we artificially shift one of the Al atoms (by 0.39 Å) in the unit cell along the a axis, as illustrated in Fig. 5(a). This breaks $\mathcal{P}$ but preserves $\mathcal{M}_z$. As a result, we find that the nodal loop is preserved and still lies in the $k_z = 0$ plane [see Fig. 5(c)]. In the second case, we artificially shift the two Al atoms along the c axis (by 0.23 Å) in the opposite directions [see Fig. 5(b)], which preserves $\mathcal{P}$ but breaks $\mathcal{M}_z$. We find that the loop is again

preserved, but its shape gets distorted and no longer lies in the $k_z = 0$ plane, as shown in Fig. 5(d). From the discussion, we see that the loop enjoys double protection. Moreover, the $\mathcal{P}$ and $\mathcal{M}_z$ symmetries are not easy to destroy by lattice strains. Such robustness would be advantageous for experimental studies and possible applications.

To further characterize the nodal loop, we construct a low-energy effective model around the Γ point. From symmetry analysis, we find that the states at Γ of the two crossing bands belong to the A_{2u} and A_{1g} irreducible representations of the D_{6h} point group. Using these two states as a basis and with the constraints from the D_{6h} and $\mathcal{T}$ symmetries [64], we can construct the $k \cdot p$ Hamiltonian for the two bands around the Γ point:

$$\mathcal{H} = \begin{bmatrix} h_{11} & h_{12} \\ h_{21} & h_{22} \end{bmatrix}, \tag{1}$$

with

$$h_{ii} = A_i\left(k_x^2 + k_y^2\right) + B_i k_z^2 + M_i, \tag{2}$$

$$h_{12} = -h_{21} = iCk_z. \tag{3}$$

Here, the wave vector $\boldsymbol{k}$ is measured from Γ, the expansion is up to k quadratic terms, and the real coefficients A_i, B_i, M_i $(i = 1,2)$, and C are material-specific parameters. The model describes a nodal loop in the $k_z = 0$ plane when $M_1 > M_2$, $A_1 < 0$, and $A_2 > 0$. From the model, we see that the two bands are decoupled in the $k_z = 0$ plane because they have opposite $\mathcal{M}_z$ eigenvalues, and the band ordering is inverted around Γ, consistent with our previous discussions. The model parameters can be obtained by fitting the DFT band structure. We find that $A_1 = -9.66$ eV Å^2, $A_2 = 11.37$ eV Å^2, $B_1 = 36.22$ eV Å^2, $B_2 = -25.71$ eV Å^2, $C = 22.34$ eV Å^2, $M_1 = 0.12$ eV, and $M_2 = -0.52$ eV for Ti_3Al, satisfying the conditions above for having a nodal loop.

B. Nodal surface

Now let us turn to discuss the degenerate bands along the A-L-H-A path in the $k_z = \pi$ plane. An enlarged view with the orbital projection is shown in Fig. 6(a). In fact, we check that all the bands in the $k_z = \pi$ plane are doubly degenerate (without counting spin). The degeneracy is due to the linear crossing between two bands along the k_z direction [see Figs. 6(b) and 6(c) for the crossing at a generic k point in the plane]. Thus, there exists a nodal surface in the $k_z = \pi$ plane formed by the crossing between the two bands. As we mentioned earlier, the presence of the nodal surface is dictated by the nonsymmorphic $\mathcal{S}_{2z}$ symmetry and $\mathcal{T}$ symmetry. To understand this point, we note that in the absence of SOC [47],

$$(\mathcal{T}\mathcal{S}_{2z})^2 = T_{001} = e^{-ik_z}, \tag{4}$$

where T_{001} is the translation along the z direction by a lattice constant. In the $k_z = \pi$ plane, each k point is invariant under the $\mathcal{T}\mathcal{S}_{2z}$ operation, and $(\mathcal{T}\mathcal{S}_{2z})^2 = -1$ means that there is a Kramers-like degeneracy due to the antiunitary $\mathcal{T}\mathcal{S}_{2z}$ symmetry. Thus, the bands in the $k_z = \pi$ plane must become doubly degenerate, forming the nodal surface. A similar argument has been presented in the previous discussion of the materials

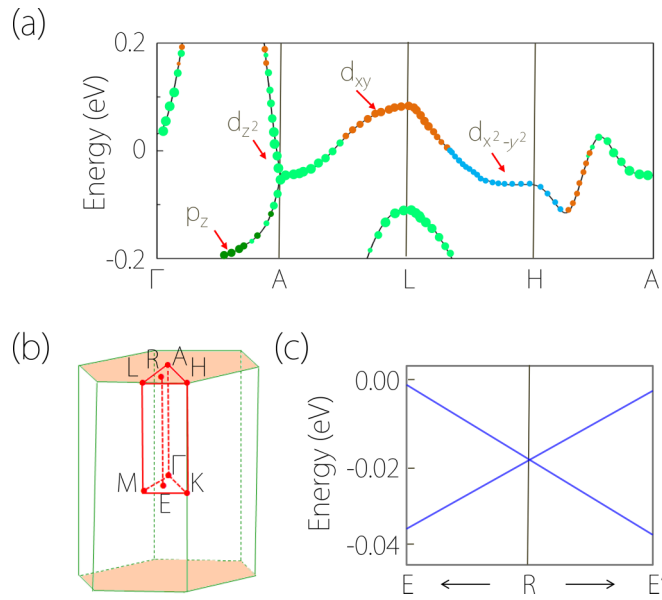

FIG. 6. (a) Orbital-projected band structure of Ti_3Al for Γ-A and paths in the $k_z = \pi$ plane. (b) shows the Brillouin zone. R and E are the centers of the triangles A-L-H and Γ-M-K, respectively. (c) Enlarged view of the low-energy band dispersion along the E-R path, showing the linear crossing between two bands along the k_z direction.

$BaVS_3$ and K_6YO_4 [46,47]. Although symmetry requires the presence of the nodal surface and confines its location in the $k_z = \pi$ plane, it puts no constraint on the energy and the dispersion of the surface. Fortunately, the nodal surface in Ti_3Al lies close to the Fermi energy, and its energy variation is relatively small [see Fig. 6(a)]. These features would facilitate the experimental studies of the nodal surface in Ti_3Al.

IV. DISCUSSION AND CONCLUSION

From the above discussion, we see that Ti_3Al hosts both a nodal loop and a nodal surface in its low-energy band structure. Since the loop lies in the $k_z = 0$ plane, while the surface is in the $k_z = \pi$ plane, the low-energy quasiparticles around the two, namely, the nodal loop fermions and the nodal surface fermions, would behave almost independently under smooth perturbation due to their large momentum separation. Hence, for such a case, they would contribute separately to physical properties. For example, regarding transport, the nodal surface fermions should exhibit very strong anisotropy: the band structure is more dispersive along the z direction than in the xy plane (the nodal surface fermions may be regarded as 1D chiral fermions in the z direction [47]). Thus, we can expect that the transport in the z direction is dominated by the nodal surface fermions (due to the much larger carrier population), whereas the transport in the xy plane would be dominated by the nodal loop fermions. The magnetic quantum oscillations are also expected to show distinct signatures for the two types of fermions. For a nodal surface relatively flat in energy, the equienergy surfaces around it would take the shape of sheets normal to z and traversing the BZ. In comparison, the equienergy surfaces around a type-I loop are tori. Thus, under a magnetic field, the nodal loop fermions

would form closed cyclotron orbits and contribute to the quantum oscillations (like de Haas–van Alphen oscillation) [44], whereas the nodal surface fermions would likely form open orbits and not contribute to the oscillation [65]. It should also be mentioned that at sharp interfaces or atomic-scale defects, scattering with large momentum transfer is possible, which may convert the carriers between the nodal loop and the nodal surface.

We have several remarks before closing. First, considering that the GGA approach sometimes overestimates the degree of band inversion, we have verified the band inversion feature for Ti_3Al by using the more accurate hybrid functional (HSE06) approach [66,67]. As shown in Fig. S2 of the Supplemental Material [68], we observe that the band inversion feature and the nodal loop are still preserved.

Second, in the above discussion, SOC is neglected. The presented symmetry arguments apply in the absence of SOC. The inclusion of SOC will, in general, gap the nodal loop and the nodal surface. Nevertheless, the opened gap is very small due to the small SOC strength in this material. Our computations indicate that the SOC gap opened at the nodal loop and the nodal surface is less than 5 meV [68], which is indeed negligible.

Third, nodal loops can also be classified based on how they wind around the BZ [35], which has the topology of a three-torus. Hence, a nodal loop that traverses the BZ is topologically distinct from a loop that does not. The distinction can be characterized by three integers (a $\mathbb{Z}^3$ index), corresponding to the number of times that the loop winds around the BZ in each of the three directions [35]. In this sense, the nodal loop here has a (0,0,0) characterization; that is, it does not traverse the BZ. Consequently, it can, in principle, be continuously deformed into a point and annihilated without breaking the symmetry of the system. Physically, this corresponds to the process in which the two crossing bands are pulled apart. In comparison, the nodal surface cannot be removed since they are guaranteed by the nonsymmorphic space-group symmetry, as we discussed above.

Fourth, nodal loop metals often possess nontrivial drum-headlike surface states on the surfaces where the loops have finite surface-projected area [16,17]. For Ti_3Al, the nodal loop lies in the $k_z = 0$ plane, so the (001) surface should host surface states. However, the nodal surface in the $k_z = \pi$ plane appears in the same energy range as the loop; hence, the surface states would largely be buried in the projection of the bulk bands [68]. Thus, the surface states here may not be easily detected in experiment.

Finally, we point out that Ti_3Al enjoys other excellent material properties. (i) Ti_3Al is easy to synthesize, and high-quality samples have been demonstrated [57–59]. (ii) Ti_3Al is stable and possesses outstanding mechanical properties [48]. The nodal loop and nodal surface features are also found in other materials of this family, including Ti_3Ga, Ti_3Sn, and Ti_3Pb (see the Supplemental Material [68]), although for some of the materials, the crossings are away from the Fermi level.

In conclusion, we have proposed that the Ti_3Al family of compounds is a new type of topological material. The material has a nodal loop in the $k_z = 0$ plane and a nodal surface in the $k_z = \pi$ plane. Both features are close to the Fermi level. Remarkably, the nodal loop is almost flat in energy, with very small energy variation (<0.25 meV), much smaller than other nodal loop materials proposed to date. The nodal loop enjoys a double-symmetry protection by either the $\mathcal{PT}$ symmetry or the $\mathcal{M}_z$ symmetry. The nodal surface is formed by the linear crossing between two low-energy bands in the entire $k_z = \pi$ plane and is guaranteed by the nonsymmorphic screwrotational symmetry and the $\mathcal{T}$ symmetry. We have constructed an effective model for describing the nodal loop and discussed the possible physical signatures due to the nodal loop and nodal surface fermions. This family of materials also possesses other excellent material properties, including high stability and excellent mechanical properties, which make these materials promising candidates to explore the interesting physics associated with the nodal loop and nodal surface metals.

ACKNOWLEDGMENTS

The authors thank Haifeng Yang, S. Wu, and D. L. Deng for valuable discussions. This work is supported by the Special Foundation for Theoretical Physics Research Program of China (Grant No. 11747152) and Singapore Ministry of Education Academic Research Fund Tier 2 (Grant No. MOE2015-T2-2-144). We acknowledge computational support from the Texas Advanced Computing Center and the National Supercomputing Centre Singapore.

[1] M. Z. Hasan and C. L. Kane, Rev. Mod. Phys. **82**, 3045 (2010).
[2] X.-L. Qi and S.-C. Zhang, Rev. Mod. Phys. **83**, 1057 (2011).
[3] A. Bansil, H. Lin, and T. Das, Rev. Mod. Phys. **88**, 021004 (2016).
[4] C.-K. Chiu, J. C. Teo, A. P. Schnyder, and S. Ryu, Rev. Mod. Phys. **88**, 035005 (2016).
[5] N. P. Armitage, E. J. Mele, and A. Vishwanath, Rev. Mod. Phys. **90**, 015001 (2018).
[6] X. Wan, A. M. Turner, A. Vishwanath, and S. Y. Savrasov, Phys. Rev. B **83**, 205101 (2011).
[7] S. Murakami, New J. Phys. **9**, 356 (2007).
[8] H. B. Nielsen and M. Ninomiya, Phys. Lett. B **130**, 389 (1983).
[9] D. T. Son and B. Z. Spivak, Phys. Rev. B **88**, 104412 (2013).
[10] S. Guan, Z.-M. Yu, Y. Liu, G.-B. Liu, L. Dong, Y. Lu, Y. Yao, and S. A. Yang, npj Quantum Mater. **2**, 23 (2017).
[11] G. E. Volovik, *The Universe in a Helium Droplet* (Oxford University Press, Oxford, 2003).
[12] S. M. Young, S. Zaheer, J. C. Y. Teo, C. L. Kane, E. J. Mele, and A. M. Rappe, Phys. Rev. Lett. **108**, 140405 (2012).
[13] Z. Wang, H. Weng, Q. Wu, X. Dai, and Z. Fang, Phys. Rev. B **88**, 125427 (2013).
[14] Y. X. Zhao and Z. D. Wang, Phys. Rev. Lett. **110**, 240404 (2013).
[15] Y. Du, F. Tang, D. Wang, L. Sheng, E.-J. Kan, C.-G. Duan, S. Y. Savrasov, and X. Wan, npj Quantum Mater. **2**, 3 (2017).
[16] H. Weng, Y. Liang, Q. Xu, R. Yu, Z. Fang, X. Dai, and Y. Kawazoe, Phys. Rev. B **92**, 045108 (2015).

[17] S. A. Yang, H. Pan, and F. Zhang, Phys. Rev. Lett. **113**, 046401 (2014).

[18] K. Mullen, B. Uchoa, and D. T. Glatzhofer, Phys. Rev. Lett. **115**, 026403 (2015).

[19] Y. Chen, Y. Xie, S. A. Yang, H. Pan, F. Zhang, M. L. Cohen, and S. Zhang, Nano Lett. **15**, 6974 (2015).

[20] Y. Kim, B. J. Wieder, C. L. Kane, and A. M. Rappe, Phys. Rev. Lett. **115**, 036806 (2015).

[21] R. Yu, H. Weng, Z. Fang, X. Dai, and X. Hu, Phys. Rev. Lett. **115**, 036807 (2015).

[22] L. S. Xie, L. M. Schoop, E. M. Seibel, Q. D. Gibson, W. Xie, and R. J. Cava, APL Mater. **3**, 083602 (2015).

[23] Z.-M. Yu, Y. Yao, and S. A. Yang, Phys. Rev. Lett. **117**, 077202 (2016).

[24] T.-T. Zhang, Z.-M. Yu, W. Guo, D. Shi, G. Zhang, and Y. Yao, J. Phys. Chem. Lett. **8**, 5792 (2017).

[25] X. M. Zhang, L. Jin, X. F. Dai, and G. D. Liu, J. Phys. Chem. Lett. **8**, 4814 (2017).

[26] X. M. Zhang, L. Jin, F. X. Dai, and G. D. Liu, Appl. Phys. Lett. **112**, 122403 (2018).

[27] Y. Chen, Y.-M. Lu, and H.-Y. Kee, Nat. Commun. **6**, 6593 (2015).

[28] R. H. Li, H. Ma, X. Cheng, S. Wang, D. Li, Z. Zhang, Y. Li, and X.-Q. Chen, Phys. Rev. Lett. **117**, 096401 (2016).

[29] G. Bian, T.-R. Chang, R. Sankar, S.-Y. Xu, H. Zheng, T. Neupert, C.-K. Chiu, S.-M. Huang, G. Chang, I. Belopolski, D. S. Sanchez, M. Neupane, N. Alidoust, C. Liu, B. Wang, C.-C. Lee, H.-T. Jeng, C. Zhang, Z. Yuan, S. Jia, A. Bansil, F. Chou, H. Lin, and M. Z. Hasan, Nat. Commun. **7**, 10556 (2016).

[30] C. Fang, H. Weng, X. Dai, and Z. Fang, Chin. Phys. B **25**, 117106 (2016).

[31] L.-Y. Gan, R. Wang, Y. J. Jin, D. B. Ling, J. Z. Zhao, W. P. Xu, J. F. Liu, and H. Xu, Phys. Chem. Chem. Phys. **19**, 8210 (2017).

[32] X. Zhang, Z.-M. Yu, X.-L. Sheng, H. Y. Yang, and S. A. Yang, Phys. Rev. B **95**, 235116 (2017).

[33] S. Li, Y. Liu, S.-S. Wang, Z.-M. Yu, S. Guan, X.-L. Sheng, Y. G. Yao, and S. A. Yang, Phys. Rev. B **97**, 045131 (2018).

[34] R. Yu, Q. Wu, Z. Fang, and H. Weng, Phys. Rev. Lett. **119**, 036401 (2017).

[35] S. Li, Z.-M. Yu, Y. Liu, S. Guan, S.-S. Wang, X. Zhang, Y. Yao, and S. A. Yang, Phys. Rev. B **96**, 081106(R) (2017).

[36] T. Bzdusek, Q. S. Wu, A. Rüegg, M. Sigrist, and A. A. Soluyanov, Nature (London) **538**, 75 (2016).

[37] S.-S. Wang, Y. Liu, Z.-M. Yu, X.-L. Sheng, and S. A. Yang, Nat. Commun. **8**, 1844 (2017).

[38] C. Zhong, Y. Chen, Z.-M. Yu, Y. Xie, H. Wang, S. A. Yang, and S. Zhang, Nat. Commun. **8**, 15641 (2017).

[39] W. Chen, H.-Z. Lu, and J.-M. Hou, Phys. Rev. B **96**, 041102 (2017).

[40] G. Chang, S.-Y. Xu, X. Zhou, S.-M. Huang, B. Singh, B. Wang, I. Belopolski, J. Yin, S. Zhang, A. Bansil, H. Lin, and M. Z. Hasan, Phys. Rev. Lett. **119**, 156401 (2017).

[41] Z. Yan, R. Bi, H. Shen, L. Lu, S.-C. Zhang, and Z. Wang, Phys. Rev. B **96**, 041103 (2017).

[42] P.-Y. Chang and C.-H. Yee, Phys. Rev. B **96**, 081114 (2017).

[43] X. Sheng, Z. Yu, R. Yu, H. Weng, and A. S. Yang, J. Phys. Chem. Lett. **8**, 3506 (2017).

[44] X. M. Zhang, Z.-M. Yu, Y. H. Lu, X.-L. Sheng, H. Y. Yang, and S. A. Yang, Phys. Rev. B **97**, 125143 (2018).

[45] C. Zhong, Y. Chen, Y. Xie, S. A. Yang, M. L. Cohen, and S. B. Zhang, Nanoscale **8**, 7232 (2016).

[46] Q.-F. Liang, J. Zhou, R. Yu, Z. Wang, and H. Weng, Phys. Rev. B **93**, 085427 (2016).

[47] W. Wu, Y. Liu, S. Li, C. Zhong, Z.-M. Yu, X.-L. Sheng, Y. X. Zhao, and S. A. Yang, Phys. Rev. B **97**, 115125 (2018).

[48] N. S. Stoloff, C. T. Liu, and S. C. Deevi, Intermetallics **8**, 1313 (2000).

[49] G. Kresse and D. Joubert, Phys. Rev. B **59**, 1758 (1999).

[50] G. Kresse and J. Hafner, Phys. Rev. B **47**, 558 (1993).

[51] J. P. Perdew, K. Burke, and M. Ernzerhof, Phys. Rev. Lett. **77**, 3865 (1996).

[52] P. E. Blöchl, Phys. Rev. B **50**, 17953 (1994).

[53] N. Marzari and D. Vanderbilt, Phys. Rev. B **56**, 12847 (1997).

[54] A. A. Mostofi, J. R. Yates, Y.-S. Lee, I. Souza, D. Vanderbilt, and N. Marzari, Comput. Phys. Commun. **178**, 685 (2008).

[55] M. P. L. Sancho, J. M. L. Sancho, and J. Rubio, J. Phys. F **14**, 1205 (1984).

[56] Q. S. Wu, S. N. Zhang, H.-F. Song, M. Troyer, and A. A. Soluyanov, Comput. Phys. Commun. **224**, 405 (2018).

[57] S. Chen, Y. Chen, H. Zhang, Y. Tang, J. Wei, and W. Sun, J. Nanomater. **2013**, 569537 (2013).

[58] K. L. Yang, J. C. Huang, and Y. N. Wang, Acta Mater. **51**, 2577 (2003).

[59] E. A. Basuki, M. Yuliansyah, F. M. Rahman, F. Muhammad, and D. Prajitno, J. Eng. Technol. Sci. **48**, 534 (2016).

[60] A. Bilic, M. A. Gibson, N. Wilson, and K. McGregor, J. Appl. Phys. **121**, 025105 (2017).

[61] T. Hong, T. J. Watson-Yang, X.-Q. Guo, A. J. Freeman, T. Oguchi, and J.-H. Xu, Phys. Rev. B **43**, 1940 (1991).

[62] T. Novoselova, S. Malinov, W. Sha, and A. Zhecheva, Mater. Sci. Eng. A **371**, 103 (2004).

[63] A. Patselov, M. Milyaev, and R. Eshchenko, Solid State Phenom. **190**, 213 (2012).

[64] C. J. Bradley and A. P. Cracknell, *The Mathematical Theory of Symmetry in Solids* (Clarendon, Oxford, 1972).

[65] D. Shoenberg, *Magnetic Oscillations in Metals* (Cambridge University Press, Cambridge, 1984).

[66] J. Heyd, G. E. Scuseria, and M. Ernzerhof, J. Chem. Phys. **118**, 8207 (2003).

[67] J. Heyd, G. E. Scuseria, and M. Ernzerhof, J. Chem. Phys. **124**, 219906 (2006).

[68] See Supplemental Material at http://link.aps.org/supplemental/10.1103/PhysRevB.97.235150 for band structure with the GGA + U method for Ti_3Al, band structure under the HSE06 calculation for Ti_3Al, band structure under SOC for Ti_3Al, projected band structure for the Ti_3Al (001) surface, and band structures for Ti_3Ga, Ti_3Sn, and Ti_3Pb.